Chromosome Image Enhancement Using Multiscale Differential Operators

Yu-Ping Wang*, *Member, IEEE*, Qiang Wu, *Member, IEEE*, Kenneth R. Castleman, *Member, IEEE*, and Zixiang Xiong, *Senior Member, IEEE*

Abstract—Chromosome banding patterns are very important features for karyotyping, based on which cytogenetic diagnosis procedures are conducted. Due to cell culture, staining, and imaging conditions, image enhancement is a desirable preprocessing step before performing chromosome classification. In this paper, we apply a family of differential wavelet transforms (Wang and Lee, 1998), (Wang, 1999) for this purpose. The proposed differential filters facilitate the extraction of multiscale geometric features of chromosome images. Moreover, desirable fast computation can be realized. We study the behavior of both banding edge pattern and noise in the wavelet transform domain. Based on the fact that image geometrical features like edges are correlated across different scales in the wavelet representation, a multiscale point-wise product (MPP) is used to characterize the correlation of the image features in the scale-space. A novel algorithm is proposed for the enhancement of banding patterns in a chromosome image. In order to compare objectively the performance of the proposed algorithm against several existing image-enhancement techniques, a quantitative criteria, the contrast improvement ratio (CIR), has been adopted to evaluate the enhancement results. The experimental results indicate that the proposed method consistently outperforms existing techniques in terms of the CIR measure, as well as in visual effect. The effect of enhancement on cytogenetic diagnosis is further investigated by classification tests conducted prior to and following the chromosome image enhancement. In comparison with conventional techniques, the proposed method leads to better classification results, thereby benefiting the subsequent cytogenetic diagnosis.

Index Terms—B-splines, chromosome karyotyping, contrast improvement ratio, differential operators, image enhancement, scale-space, wavelets.

I. INTRODUCTION

THE BANDING patterns of chromosomes constitute very important features for cytogeneticists to classify different types of chromosomes and, thus, produce a karyotype [3]. Based on chromosome karyotyping, clinical diagnostic procedures can be performed. Due to the presence of noise and other sources of distortion resulting from poor sample preparation, imaging and
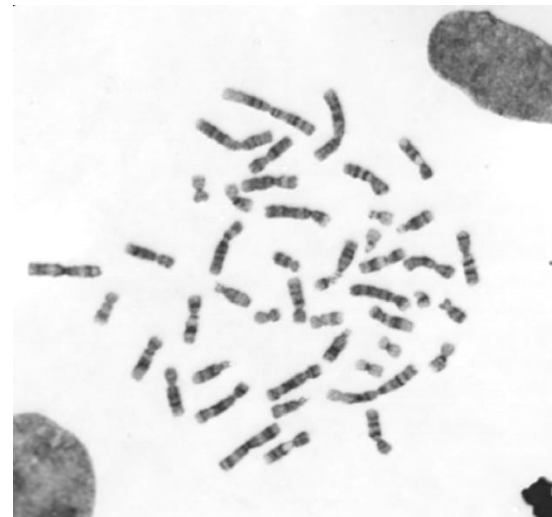
*Y.-P. Wang is with the Advanced Digital Imaging Research, LLC., 2525 South Shore Blvd., Suite 100, League City, TX 77573 USA (e-mail: wyp@adires.com).
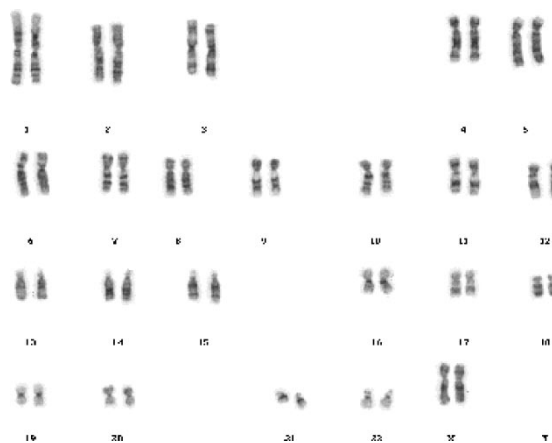
Q. Wu and K. R. Castleman are with the Advanced Digital Imaging Research, LLC, League City, TX 77573 USA.

Z. Xiong is with the Electrical Engineering Department, Texas A&M University, College Station, TX 77843 USA.

(a)

(b)

Fig. 1. A chromosome spread image (a) and its karyotype (b).

digital quantization, vague, low-contrast band patterns are usually obtained in the image. Therefore, enhancement of these patterns is desirable before band descriptors are extracted [4]. As an example, from the chromosome images in Fig. 1, it can be seen that banding patterns are transverse image features, perpendicular to the medial axis of the chromosome. These geometric features require image transforms that can facilitate their extraction. Laplacian filtering has been used for extraction of these banding features [3].

The aim of image enhancement is to improve the visibility of low-contrast features while suppressing noise. Among various techniques, differential or difference operators have long

been used for image enhancement because they facilitate the extraction of important geometric features like edges. For instance, image sharpening techniques use the gradient information given by the Sobel, Roberts, and/or compass operators [5]. An adaptive method was reported on mammographic image enhancement based on the first derivative [6]. Since differential operators can be regarded as high-pass filters, these techniques actually sharpen the image by extrapolating its high-frequency information.

Since geometric features in an image are known to occur at multiple scales, multiscale differential operators can be used for image enhancement. Among them, the derivative of Gaussian has received considerable attention. This operator estimates the gradient of an image after smoothing it with a Gaussian function. The Laplacian pyramid, on the other hand, is one of the variants that has also been used for image enhancement [7]. Because human eyes are known to be anisotropic in their sensitivity to details along different orientations, two-directional Laplacian operators are employed in an adaptive unsharp masking algorithm in [8]. Contrast enhancement based on a multiscale gradient operator has also been studied in [9]. In [10] and [11], mammographic and echocardiogram image enhancement utilizing multiscale differential wavelets have also been reported. The wavelet transform in some sense can be regarded as a differential operation, and for this reason it also has been used for medical image enhancement [12], [13].

Motivated by the close approximation of B-spline bases to Gaussian and wavelet theory, in [1] and [2], we presented a formal framework for multiscale image representations using differential operators. Besides Laplacian operators, which are isotropic, different kinds of wavelets were designed for multiscale differential representations of images. These include gradient operators and multidirectional operators. An image can be decomposed and reconstructed from its differential components at multiple scales. By taking advantage of the spline properties, a fast algorithm was derived in [2]. The resulting wavelet representations are different from the usual wavelet models in that they are over-complete and translation invariant. It is shown in [14], that thresholding in a translation invariant wavelet domain can eliminate unpleasant artifacts introduced by modification of orthogonal wavelet expansion coefficients. In general, these over-complete representations are more flexible than orthogonal representations and are more suitable for geometry-based image processing.

In this paper, we make use of our differential representations for chromosome image enhancement by exploiting the geometric correlation of image features in these domains. The remainder of this paper is organized as follows. In Section II, we introduce a class of wavelets with which an image can be represented by its second-order derivatives. Specifically, the filters used for both decomposition and reconstruction are given. In Section III, we analyze the characteristics of edges in these scale-space representations and their cross-scale correlations. A novel enhancement scheme is proposed. It makes use of cross-scale statistics to enhance the salient features of an image. Section IV presents the experimental results. In particular, we compare the objective performance of the proposed method with that of several conventional enhancement methods, using the
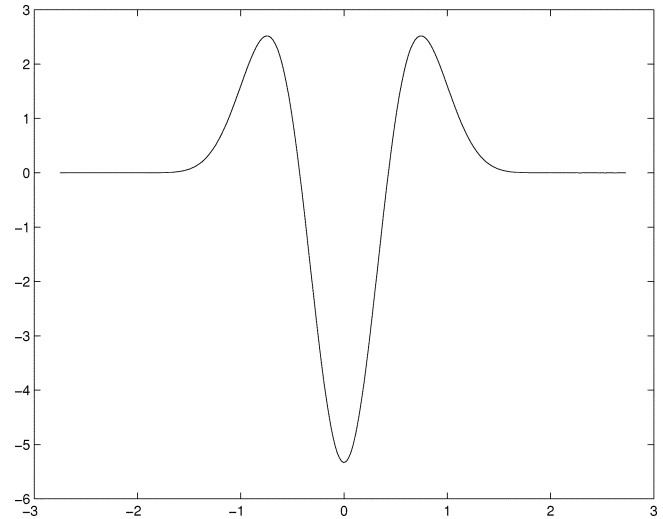

Fig. 2. A cubic B-spline wavelet, which is the second derivative of a cubic B-spline.

criterion of contrast improvement ratio (CIR). In order to evaluate further the effectiveness of the proposed enhancement algorithm, Section V compares the chromosome classification results following various enhancement methods. Section VI concludes the paper.

II. MULTIRESOLUTION DIFFERENTIAL REPRESENTATIONS OF IMAGES

A family of wavelets which are the derivatives of splines are designed in [2]. An image can be synthesized from its derivative components at multiple scales. These differential operators include gradient, Laplacian, second derivative and multidirectional operators. At each scale, these operators resemble the Sobel, the Roberts and the compass operators [5]. As shown in [15], filters of different sizes and directions are usually needed to prevent edge blurring. In this section, we review the wavelet representation for second derivative operators, which are used in this paper. More details can be found in [1] and [2].

In the one-dimensional (1-D) case, a differential wavelet which resembles the Mexican-hat or Laplacian of Gaussian (LoG) wavelet is defined as the second derivative of B splines of different order.

$$\psi^n(x) = \frac{1}{4}\frac{d^2}{dx^2}\beta_{2^{-1}}^{n+2}(x)$$
$$= 2\left(\beta^n(2x+1) - 2\beta^n(2x) + \beta^n(2x-1)\right). \quad (1)$$

The cubic spline wavelet shown in Fig. 2 is of order $n = 3$, and is symmetric with respect to the origin. The definitions of B-splines and its good properties can be found in [16].

The wavelet transform is defined as

$$W_{2^j}f = f * \psi_{2^j}^n, \quad j = 1, 2, \cdots, J \quad (2)$$

If we introduce the smoothing operations $S_{2^j}f = f * \beta_{2^j}^n$, $j = 1, 2, \cdots, J$, it can be shown that the above wavelet transforms are the second derivatives of smoothing operations.

A multiscale representation of an image can be obtained by convoluting of the image with a two-dimensional (2-D) smoothing function defined as $\beta^n(x,y) = \beta^n(x)\beta^n(y)$ at different scales. For discrete implementation, we approximate the three directional derivative components or wavelet decompositions by

$$
\begin{cases}
W^1_{2^j}f(x,y) = \frac{1}{4}\dfrac{\partial^2\left(f*\left(\beta^{n+2}_{2^j-1}(x)\beta^n_{2^j-1}(y)\right)\right)}{\partial x^2} = (f*\psi^{n,1})(x,y) \\[4mm]
W^2_{2^j}f(x,y) = \frac{1}{4}\dfrac{\partial^2\left(f*\left(\beta^n_{2^j-1}(x)\beta^{n+2}_{2^j-1}(y)\right)\right)}{\partial y^2} = (f*\psi^{n,2})(x,y) \\[4mm]
W^3_{2^j}f(x,y) = \frac{1}{4}\dfrac{\partial^2\left(f*\left(\beta^{n+1}_{2^j-1}(x)\beta^{n+1}_{2^j-1}(y)\right)\right)}{\partial x\,\partial y} = (f*\psi^{n,3})(x,y).
\end{cases}
\tag{3}
$$

As a clarification, in the original definition of the above formula in [1] and [2], there was an error. Here, we actually use the approximation formula to compute the second directional derivative components for the sake of deriving the recursive formula. From this formula, the three directional wavelets are defined as

$$
\hat{\psi}^{n,1}(2\omega_x,2\omega_y) = G^{(2)}(\omega_x)\hat{\beta}^n(\omega_x,\omega_y)
$$
$$
\hat{\psi}^{n,2}(2\omega_x,2\omega_y) = G^{(2)}(\omega_y)\hat{\beta}^n(\omega_x,\omega_y)
$$
$$
\hat{\psi}^{n,3}(2\omega_x,2\omega_y) = G^{(1)}(\omega_x)G^{(1)}(\omega_y)\hat{\beta}^n(\omega_x,\omega_y)
$$

where we denote by $G^{(1)}$ and $G^{(2)}$ the transfer functions of the first- and second-order difference operators $g^{(1)}$ and $g^{(2)}$.

By taking advantage of the refinability property of the splines, we can obtain a recursive algorithm for the computation of these three local partial derivatives along the dyadic scales $\{2^j\}_{j\in\mathbb{Z}}$. Consequently, we have the following **discrete decomposition formula**:

$$
\begin{cases}
S_{2^j}f = S_{2^{j-1}}f*(h,h)_{\uparrow 2^{j-1}} \\[2mm]
W^1_{2^j}f = S_{2^{j-1}}f*\left(g^{(2)},d\right)_{\uparrow 2^{j-1}} \\[2mm]
W^2_{2^j}f = S_{2^{j-1}}f*\left(d,g^{(2)}\right)_{\uparrow 2^{j-1}} \\[2mm]
W^3_{2^j}f = S_{2^{j-1}}f*\left(g^{(1)},g^{(1)}\right)_{\uparrow 2^{j-1}}
\end{cases}
\tag{4}
$$

where $I*(h,g)_{\uparrow 2^{j-1}}$ represents the separable convolution of the rows and columns of the image with the 1-D filters $[h]_{\uparrow 2^{j-1}}$ and $[g]_{\uparrow 2^{j-1}}$, respectively. The symbol d denotes the Dirac filter whose impulse is one at the origin and zero elsewhere. The up-sampling operation of a sequence $\{h(n)\}$ by an integer factor m is defined as $[h]_{\uparrow m}$.

One can reconstruct the image by using the following **discrete reconstruction formula**:

$$
S_{2^{j-1}}f = W^1_{2^j}f*\left(\tilde{g}^{(2)},u\right)_{\uparrow 2^{j-1}} + W^2_{2^j}f*\left(u,\tilde{g}^{(2)}\right)_{\uparrow 2^{j-1}}
$$
$$
+ W^3_{2^j}f*\left(\tilde{g}^{(1)},\tilde{g}^{(1)}\right)_{\uparrow 2^{j-1}} + S_{2^j}f*(h,h)_{\uparrow 2^{j-1}}
\tag{5}
$$

where $u(j) = (1/(2^{2n+2}))\binom{2n+2}{j}$, $0 \le j \le 2n+2$, are the finite-impulse responses (FIRs) of the transfer function $U(\omega) = H^2(\omega)$, and $\tilde{g}^{(1)}$ and $\tilde{g}^{(2)}$ are the impulse responses of $\tilde{G}^{(1)}$ and $\tilde{G}^{(2)}$.

TABLE I
FIR FILTERS FOR DECOMPOSITION AND RECONSTRUCTION BASED ON THE LINEAR SPLINES

taps	h	$\tilde{h}$	$g^{(1)}$	$g^{(2)}$	$\tilde{g}^{(1)}$	$\tilde{g}^{(2)}$	u
-2					$\frac{1}{16}$		$\frac{1}{16}$
-1	$\frac{1}{4}$	$\frac{1}{4}$	-1	$\frac{1}{2}$	$\frac{5}{16}$	$\frac{-1}{8}$	$\frac{4}{16}$
0	$\frac{1}{2}$	$\frac{1}{2}$	1	-1	$\frac{-6}{16}$	$\frac{-6}{8}$	$\frac{6}{16}$
1	$\frac{1}{4}$	$\frac{1}{4}$		$\frac{1}{2}$	$\frac{1}{16}$	$\frac{-1}{8}$	$\frac{4}{16}$
2							$\frac{1}{16}$

TABLE II
FIR FILTERS FOR DECOMPOSITION AND RECONSTRUCTION BASED ON THE CUBIC SPLINES

taps	h	$\tilde{h}$	$g^{(1)}$	$g^{(2)}$	$\tilde{g}^{(1)}$	$\tilde{g}^{(2)}$	u
-4					$\frac{1}{256}$		$\frac{1}{256}$
-3					$\frac{9}{256}$	$\frac{-1}{128}$	$\frac{8}{256}$
-2	$\frac{1}{16}$	$\frac{1}{16}$			$\frac{37}{256}$	$\frac{-10}{128}$	$\frac{28}{256}$
-1	$\frac{1}{4}$	$\frac{1}{4}$	-1	$\frac{1}{2}$	$\frac{93}{256}$	$\frac{-47}{128}$	$\frac{56}{256}$
0	$\frac{3}{8}$	$\frac{3}{8}$	1	-1	$\frac{-93}{256}$	$\frac{-140}{128}$	$\frac{70}{256}$
1	$\frac{1}{4}$	$\frac{1}{4}$		$\frac{1}{2}$	$\frac{-37}{256}$	$\frac{-47}{128}$	$\frac{56}{256}$
2	$\frac{1}{16}$	$\frac{1}{16}$			$\frac{-9}{256}$	$\frac{-10}{128}$	$\frac{28}{256}$
3					$\frac{-1}{256}$	$\frac{-1}{128}$	$\frac{8}{256}$
4							$\frac{1}{256}$

Furthermore, if we define the three corresponding reconstruction wavelets as

$$
\hat{\chi}^{n,1}(\omega_x,\omega_y) = \tilde{G}^{(2)}(\omega_x)H^2(\omega_y)\hat{\beta}^n(\omega_x,\omega_y)
$$
$$
\hat{\chi}^{n,2}(\omega_x,\omega_y) = \tilde{G}^{(2)}(\omega_y)H^2(\omega_x)\hat{\beta}^n(\omega_x,\omega_y)
$$
$$
\hat{\chi}^{n,3}(\omega_x,\omega_y) = \tilde{G}^{(1)}(\omega_x)\tilde{G}^{(1)}(\omega_y)\hat{\beta}^n(\omega_x,\omega_y)
$$

then the image $f(x,y) \in L^2(\mathbb{R}^2)$ can be recovered in continuous form from its three directional derivative components $\{W^k_{2^j}\}^{k=1,2,3}_{j\in\mathbb{Z}}$ as

$$
f(x,y) = \sum_{j=-\infty}^{\infty}\left(W^1_{2^j}f*\chi^{n,1}(x,y) + W^2_{2^j}f*\chi^{n,2}(x,y)\right.
$$
$$
\left. + W^3_{2^j}f*\chi^{n,3}(x,y)\right),\quad (x,y)\in\mathbb{R}^2.
$$

Besides translation invariance and low computational complexity, this wavelet representation has two other advantages. First, the edge components of the image are displayed in the transform domain. One can make use of this information to minimize edge blurring, which usually must be addressed by image enhancement algorithms. Second, directional adaptation can be done to overcome the limitation of conventional enhancement methods that use isotropic Laplacian operators.

In this section, we specify the discrete filters for cases of $n = 1$ and $n = 3$, as used in the decomposition and reconstruction formulas. They are listed in Tables I and II. The derivation of these filters can be found in [2].

Since all the filters $h^{(j)}$, $g^{(j)}$ consist of linear combinations of binomials, the computational efficiency can be improved by using the *Pascal triangular algorithm*, with only additions and *bit shifts* operations. The computational complexity of this approach is $\mathcal{O}(N)$ [2], where N is the size of signal. This is a significant improvement over the recursive procedures described
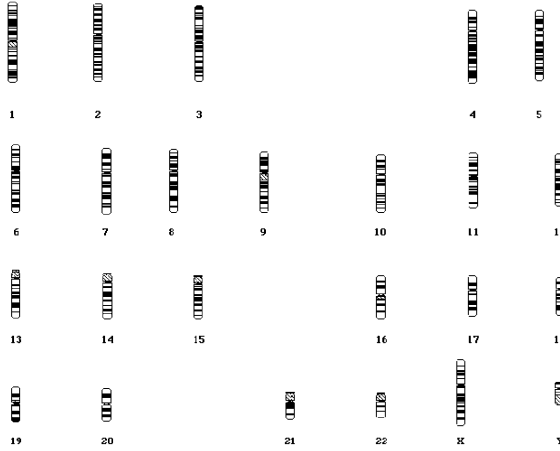
Fig. 3. Chromosomes in Fig. 1(a) are classified into 24 classes according to the banding patterns of different classes, known as the ideograms shown here.

in (4) and (5), which are of complexity $\mathcal{O}(N log_2 N)$. Also, it is easy to show that these filters allow integer to integer mapping.

III. CROSS-SCALE FEATURE CORRELATION AND THE PROPOSED ENHANCEMENT ALGORITHM

A. Chromosome Banding Patterns

Staining techniques such as Giemsa or Quinacrine, bind more specifically to certain DNA base groups than to others and, thus, produce a characteristic transverse band pattern in chromosomes. These banding patterns allow the human chromosomes to be classified into 24 different types. As an extension to the Denver nomenclature a standard ideogram system was established. It uses schematic representations to define the classification model according to the characteristic band patterns of the different chromosomes. Fig. 3 shows the ideograms of the chromosomes. The automatic procedure to identify the chromosomes in a cell according to the standard ideogram models is known as computer karyotyping. Diagnostic information can be derived from the karyotype by examining the chromosome band patterns and the overall chromosome complement, and relating any abnormalities to the clinical diagnosis.

With the advent of staining techniques that produce distinctive banding patterns, automatic chromosome recognition becomes a reality. The banding patterns are among the most important features for chromosome identification [4]. Numerous efforts have been made to utilize these features for chromosome karyotyping. The banding patterns appear as sequences of alternate dark and light bands, as shown in Fig. 3. We can model these patterns as superpositions of a set of nonoverlapped 2-D pulse or block edge signals [see (6)] with different strengths, widths, and positions. Our enhancement algorithm aims to enhance these important edge patterns.

B. Analysis of an Ideal Banding Pattern

As discussed above, the banding patterns can be formed by a set of nonoverlapped pulse patterns at different locations. For

simplicity, we begin with the 1-D case. Suppose we have the following 1-D edge pattern

$$e(x) = A \left[u \left(x + \frac{d}{2} \right) - u \left(x + \frac{d}{2} \right) \right] \qquad (6)$$

where A and d represent the magnification and width of the pulse and $u(x)$ is the step function

$$u(x) = \begin{cases} 1, & \text{if } x \geq 0 \\ 0, & \text{otherwise} \end{cases} \qquad (7)$$

The derivative of $e(x)$ is

$$e'(x) = A \left[\delta \left(x + \frac{d}{2} \right) - \delta \left(x + \frac{d}{2} \right) \right] \qquad (8)$$

In the presence of noise, we can model the pattern as

$$s(x) = e(x) + n(x) \qquad (9)$$

where $n(x)$ is a white Gaussian noise, with the auto correlation function $r_n(\tau) = E[n(t + \tau)n(t)]$ being

$$r_n(\tau) = \begin{cases} \sigma^2, & \text{if } x \geq x_0 \\ 0, & \text{otherwise} \end{cases} \qquad (10)$$

In the discrete wavelet transform domain, the above edge signal is transformed into

$$W_{2^j} s(x) = W_{2^j} e(x) + W_{2^j} n(x). \qquad (11)$$

Because of the definition of wavelets in (1), the deterministic part becomes

$$\begin{aligned} W_{2^j} e(x) &= e(x) * \frac{1}{4} \frac{d^2}{dx^2} \beta_{2^j-1}^{n+2}(x) = \frac{d}{dx} e(x) * \frac{1}{4} \frac{d}{dx} \beta_{2^j-1}^{n+2}(x) \\ &= A \left[\delta \left(x + \frac{d}{2} \right) - \delta \left(x + \frac{d}{2} \right) \right] * \frac{1}{4} \frac{d}{dx} \beta_{2^j-1}^{n+2}(x) \\ &= \frac{A}{4} \left(\frac{d}{dx} \beta_{2^j-1}^{n+1} \left(x + \frac{d}{2} \right) - \frac{d}{dx} \beta_{2^j-1}^{n+1} \left(x - \frac{d}{2} \right) \right) \\ &= \frac{A}{4} \left(\beta_{2^j-1}^{n} \left(x + \frac{d}{2} + 1 \right) - \beta_{2^j-1}^{n} \left(x + \frac{d}{2} - 1 \right) \right. \\ &\quad \left. - \beta_{2^j-1}^{n} \left(x - \frac{d}{2} + 1 \right) + \beta_{2^j-1}^{n} \left(x - \frac{d}{2} - 1 \right) \right) \end{aligned}$$

where we have used the fact that the derivative of a B-spline function is the difference of the splines of lower orders at adjacent pixels. Therefore, the wavelet transform of a pulse edge are simply the differences of two first-order derivative of B-spline functions with different smoothing sizes, as suggested in the above equation. As a result, it is easy to understand that there are two positive and negative peaks of different sizes in the transform domain, as shown in Fig. 4. In addition, strong correlation of the extrema between adjacent scales can be observed. These extrema appear to propagate across different scales while maintaining spatial correlation. Section III-C will discuss how to measure such correlation.

Let us now look at the random part in (11). It is known that a stationary random field remains stationary after convolutional and derivative operations. Furthermore, if we use the density
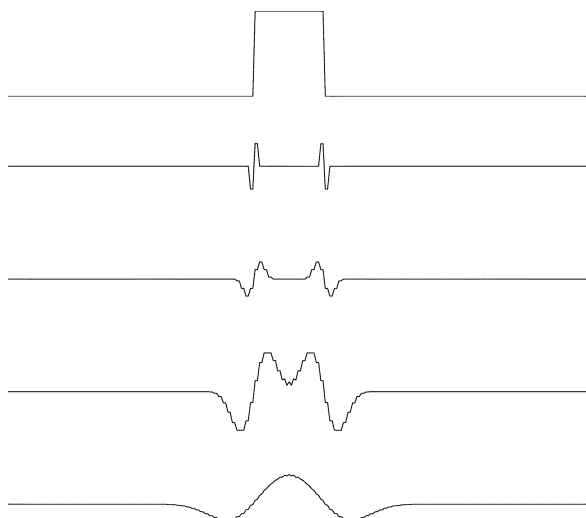
Fig. 4. Translation invariant wavelet decompositions of an ideal banding pattern model. Top row is the pulse edge model. The next four rows are the wavelet details $W_{2^j}e(x)$ at dyadic scales 1, 2, 4, and 8, which are simply the differences of two spline derivatives with different size and location.
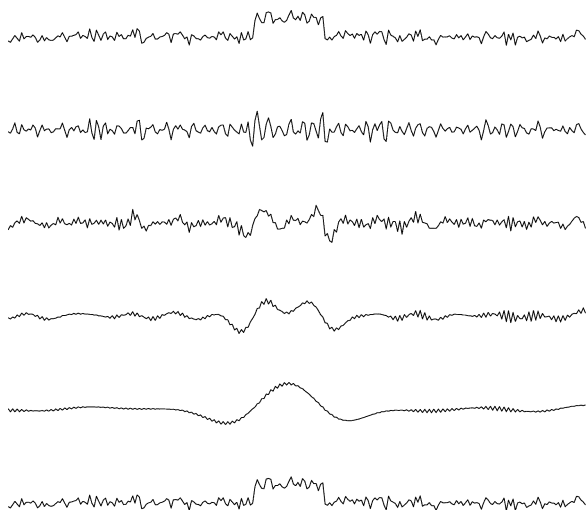
Fig. 5. Wavelet decompositions of a pulse edge model with added white noise. Top row shows the edge signal with added white noise. Bottom row shows the reconstructed signal. The intermediate rows show the wavelet details $W_{2^j}s(x)$ at dyadic scales 1, 2, 4, and 8. The white noise is smoothed out with increasing scales. Only those coefficients at edge points remain large.

of extrema to characterize the distribution of white noise in the wavelet domain, we can show that the density of maxima D_s of white noise have the following form, according to a similar analysis described in [17]:

$$D_j = \frac{\sqrt{3}}{2\pi} \frac{1}{2^j} \frac{1}{\sqrt{n+1}} \tag{12}$$

where j is the scale of smoothing and n is the order of the spline. In other words, the number of local maxima due to noise decreases quickly as the scale goes up because of increased smoothing. The average number of local maxima at 2^{j+1} is half of that at scale 2^j. Fig. 5 shows such a process, which clearly indicates that the white noise is smoothed out as the scale increases.
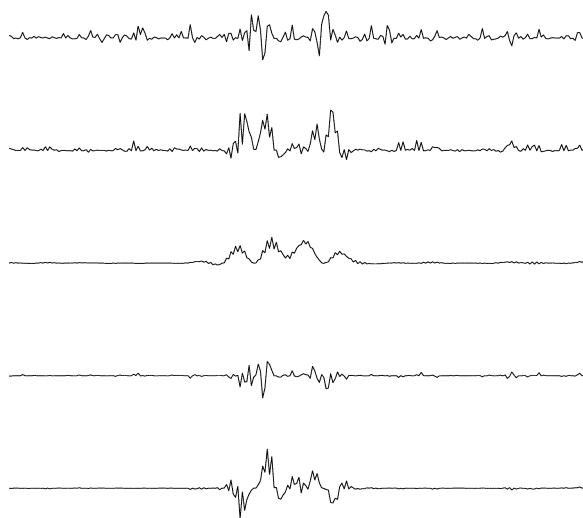
Fig. 6. MPPs for the pulse edge pattern with added noise in Fig. 5. The first three rows are the MPPs between adjacent scales 1 and 2, 2 and 4, and 4 and 8, respectively. The next two rows are the MPP between three scales, 1, 2, and 4, as well as 2, 4, and 8. From this figure it can be seen that the MPP reinforces the signal while suppressing the noise.

C. Cross-Scale Correlation Measurement: Multiscale Point-Wise Product (MPP)

Following the analysis in the previous section, we know that edges occur across different scales, and they are correlated spatially. In this paper, we have adopted the MPP to measure the cross-scale correlation. The MPP is defined as

$$p_K(n) = \prod_{j=1}^{K} W_{2^j}f(n). \tag{13}$$

This criteria was used for detection and localization [18], denoising [19], and filtering of magnetic resonance images [13]. In fact, even before the advent of wavelet transform, the MPP had been used to enhance multiscale signal peaks while suppressing noise, by exploiting the multiscale correlation of desired signals [20], [21]. Since the maxima of $W_{2^j}f(n)$ due to edges in the signal $f(n)$ tend to propagate across scales, while the maxima due to noise will not, p_K reinforces the response of the signal rather than the noise, as seen in Fig. 6. Fig. 7 shows another cross-scale product example from a synthetic signal containing various types of edges. This example indicates that the multiscale product has an inherent ability to suppress isolated and narrow impulses while preserving the edge responses across different scales.

The characterization of cross-scale correlation statistics of p_K was studied in [18]. Let y_1, y_2 be zero-mean, jointly Gaussian random variables with covariance matrix

$$C = \begin{bmatrix} \sigma_1^2 & \rho_{12}\sigma_1\sigma_2 \\ \rho_{12}\sigma_1\sigma_2 & \sigma_2^2 \end{bmatrix}$$

where ρ_{12} is the correlation coefficient. The product $z = y_1 y_2$ has the following probability density function (pdf):

$$f(z) = \frac{1}{\pi\sigma_1\sigma_2\sqrt{1-\rho_{12}^2}} e^{\rho_{12}\sigma_1\sigma_2 z} K_0\left(\sigma_1\sigma_2|z|\right)$$
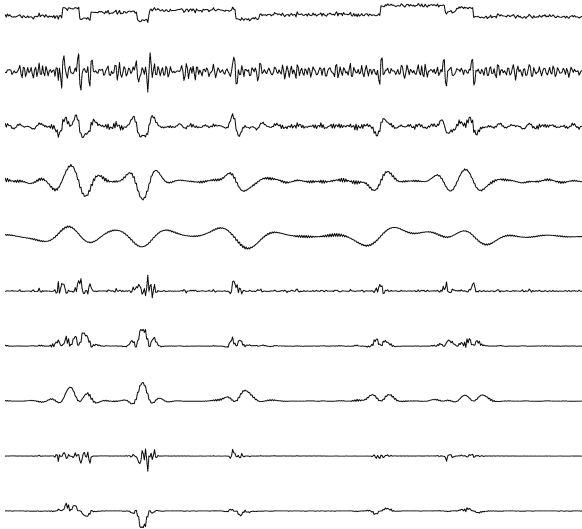
Fig. 7. Wavelet decompositions of a simulated banding block pattern using the wavelet shown in Fig. 2. Top row is the block signal with added white noise. From the second to the fifth row are the four wavelet decomposition coefficients at scale 1, 2, 4, and 8. The sixth and eighth rows are the MPP between adjacent scales. The ninth row is the MPPs between three scales (1,2, and 4). The tenth row is the MPP between three scales (2, 4, and 8). From this figure, we observe that strong correlations around edge points can be detected by the use of MPP.

where K_0 is the modified Bessel function of the second kind and zero order. The resulting PDFs are generally non-Gaussian and heavily tailed. The plots of these PDFs in [18] indicate there is a relatively sharp peak at the origin. Therefore, it is easy to understand why most MPP values are zero due to this high probability of occurrence. The MPP has also been used for detection and estimation of step change locations [18].

So far, we have discussed only the cases involving 1-D signals. For 2-D signals, the MPP is sensitive to direction and is different along the horizontal, vertical, and diagonal direction. Bearing these properties in mind, we propose the following algorithm for 2-D image-enhancement.

D. Enhancement Algorithm

The proposed enhancement algorithm can be summarized by the following three steps.

1) Perform multiscale differential decompositions of an image using spline wavelets. Thus, we have a sequence of wavelet decompositions $\{W_{2^j}^d f, d = 1, 2, 3; 0 \leq j \leq J; S_{2^J} f\}$ along the horizontal, vertical, and diagonal direction. These wavelet decompositions take into account the visual sensitivity to orientation of stimulus [22]. The user interface has several options. The user can choose to modify these wavelet directional components selectively in order to highlight certain detailed information of the image.

2) Sort the values of $p_K^d(n)$, $d = 1, 2, 3$ at each pixel in increasing order. This way, one can find out which wavelet components contribute more to the image. The user sets threshold μ for different degree of enhancement. Larger
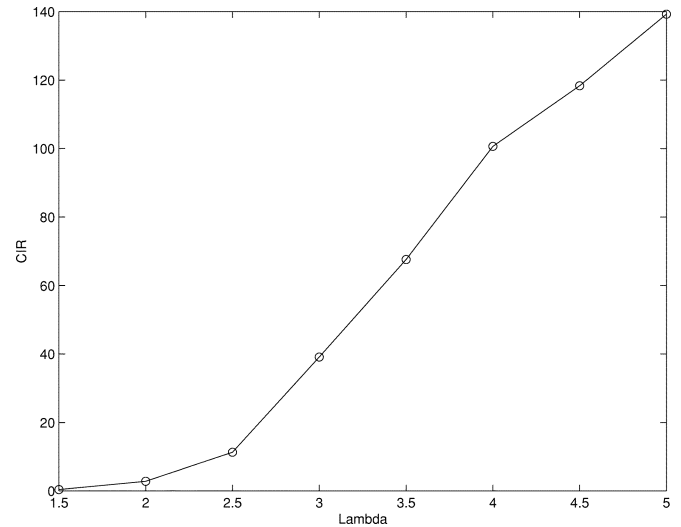

Fig. 8. Curve of the CIR as a function of the parameter lambda. It is a monotonically increasing function.
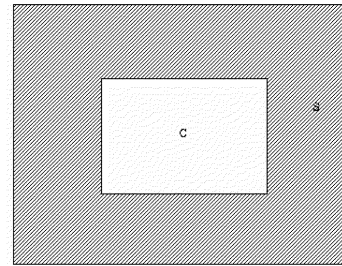

Fig. 9. Local contrast is defined as the measure between a center region (C) and a surrounding region (S). The size of the center and surrounding window is 3×3 and 7×7, respectively.

value of μ results in a high denoising effect, and *vice visa*. Thresholding is performed using the following formula:

$$\tilde{W}_{2^j}^d f(n) = \begin{cases} \lambda^{(j)} W_{2^j}^d f(n), & \text{if } \left| p_K^d(n) \right| \geq \mu \\ 0, & \text{if } \left| p_K^d(n) \right| < \mu \end{cases} \quad (14)$$

where $\lambda^{(j)}$ is an adjustable constant, corresponding to scale j. The low-frequency components of the image $S_{2^J} f$ are kept unchanged.

3) After the wavelet components are modified in steps 1 and 2, the inverse wavelet transform is performed using the reconstruction formula (5).

In (14), the choice of μ depends on the noise level in the image. This is quite similar to the hard thresholding method used in [23]. Because chromosome images used in this study have little noise, the value of μ is set to be very small. The user has the option to specify different value of $\lambda^{(j)}$ for different degree of enhancement. Fig. 8 shows the relation of the local CIR [see the definition in (16)] with this parameter. It can be shown that the higher value the $\lambda^{(j)}$ has, the greater contrast improvement the method yields. Because high-frequency components are usually displayed at low-scale resolutions, we set large $\lambda^{(j)}$ values at lower scales. At higher scales there remain low-frequency components and the location of edges may migrate due to smoothing. We, therefore, give $\lambda^{(j)}$ low values at high-scale

TABLE III
A COMPARISON OF THE CIRS FROM DIFFERENT METHODS FOR
ENHANCING THE CHROMOSOME SPREAD IMAGES

Image	CS	ACE	CGT	MCE	Wavelets
case 1	0.086815	0.348786	0.187432	1.250568	3.687726
case 2	0.027097	0.043592	0.144093	1.976530	4.070444
case 3	0.024642	0.501722	0.318388	1.241655	4.415289
case 4	0.023058	0.052394	0.316376	0.467712	3.443069
case 5	0.023384	0.075382	0.322150	6.357038	4.167665
case 6	0.027673	0.036940	0.284974	0.534539	2.795811
case 7	0.027520	0.075593	0.238987	2.303651	2.924170
case 8	0.024414	0.047069	0.309296	0.122831	5.011090
case 9	0.031110	0.037198	0.234534	3.142487	2.179077
case 10	0.015149	0.125721	0.497367	4.167377	7.150723
average	0.031086	0.134440	0.285360	2.1564	3.984506

TABLE IV
A COMPARISON OF THE CIRS FROM DIFFERENT METHODS
FOR ENHANCING THE CHROMOSOME KARYOTYPE IMAGES

Image	CS	ACE	CGT	MCE	Wavelets
case 1	0.002152	0.140547	0.251411	0.00228	11.040475
case 2	0.002506	0.159775	0.509344	0.002329	12.803198
case 3	0.002563	0.154752	0.437308	0.002303	12.803198
case 4	0.003422	0.139662	0.389644	0.001711	15.206647
case 5	0.002955	0.186505	0.668641	0.002462	16.363707
case 6	0.002896	0.163876	0.660028	0.001620	15.060397
case 7	0.002605	0.164495	0.622289	0.001782	8.903317
case 8	0.003139	0.182459	0.572494	0.002163	10.917126
case 9	0.002601	0.206372	0.684015	0.002204	9.676878
case 10	0.002622	0.165236	0.449517	0.002348	13.192122
case 11	0.009323	0.196467	0.805869	0.003231	12.435687
average	0.0033	0.1691	0.5501	0.00212	12.5821

resolutions. In our experiments, we usually set the values of $\lambda^{(j)}$ to be 5, 2, and 2 for the low-, medium-, and high-scale resolution, respectively. The software that we develop give clinicians an option to change the value of this parameter in three directions in order to visualize the details of chromosome images selectively.

For chromosome spread images, we also perform a histogram stretch to enhance the contrast of the image.

IV. RESULTS AND COMPARISONS

A. Enhancement Performance Measurement

Ordinary techniques for image contrast enhancement can be categorized generally into two types [5]. The first type is based on the image histogram and modifies the brightness of each pixel using statistical information about the image. For the second type, the high- and low-frequency components of an image are usually separated and manipulated before they are recombined. An example of this type of method is unsharp masking. Algorithms described in [6]–[8], [24], and [25] all belong to the second type.

Quantification of contrast enhancement is generally difficult. Furthermore, there is no universal measure for specifying either the objective or the subjective performance of the enhancement algorithm. Contrast is often defined as the difference in mean luminance between an object and its surrounding. There are many measures of contrast. We adopt the definition proposed in [26], where the local contrast is defined as the difference of the mean values in two rectangular windows centered on a pixel. Specifically, the local contrast $c(x, y)$ is defined as

$$c(x, y) = \frac{|p - a|}{|p + a|} \quad (15)$$

where p and a are the average values of gray levels in the center window and surrounding window of the pixel location (x, y), as illustrated in Fig. 9. It gives the contrast measure c in the range [0,1]. The performance measure CIR is defined as the ratio of the enhanced image and the original image within the region of interest R, i.e.,

$$CIR = \frac{\sum_{(x,y) \in R} |c(x,y) - \tilde{c}(x,y)|^2}{\sum_{(x,y) \in R} c(x,y)^2} \quad (16)$$

where c and $\tilde{c}$ are the local contrast values of the original and the enhanced images, respectively. In our experiments, we assume that R is the whole image.

For objective evaluation of contrast improvement, the proposed method is compared with three conventional enhancement techniques. These are the adaptive contrast stretch (ACS), the adaptive contrast enhancement (ACE), and the contrast gain transform (CGT) [27]. The CGT and ACE parameters used in [27] are 25 and 2.0 in our experiments. The λ parameters used in our proposed method for the three scales are 5, 2, and 2, respectively. In addition, we also compare with the multiscale contrast enhancement (MCE) approach proposed in [28]. Chromosome images are used in routine cytogenetic diagnosis and cancer research. Image enhancement is desired for high-resolution display and visualization of the chromosome band patterns [4]. A set of 21 human chromosome images, including 10 chromosome metaphase spread images and 11 karyotype images, were tested in the experiments. The test results, in terms of the average CIRs measured from the spread and karyotype images, are tabulated in Tables III and IV, respectively. Among all the methods tested, the proposed approach consistently yields the highest CIRs.

Fig. 10 shows one example of the spread image enhancement using different enhancement methods. One can see that the proposed wavelet method produces the best visualization effect after enhancing the band patterns. The ACE method and the CGT method, on the other hand, both cause blurring at edges.

V. EFFECT OF IMAGE ENHANCEMENT ON CHROMOSOME CLASSIFICATION

The effect of image enhancement is ultimately judged by the accuracy of downstream chromosome classification, to determine if the enhanced images result in improved karyotyping and, hence, improved diagnosis. It is well known that a normal human cell contains 46 chromosomes. The procedure to identify the chromosomes in a cell, according to the standard ideogram system, is known as karyotyping. Diagnostic information can be derived from the karyotype by examining the chromosome complement and their band patterns, and relating the numerical and structural abnormalities to biological or clinical significance. A well-known example is *Down's syndrome* (mongolism), which is characterized by the presence of three chromosomes of class
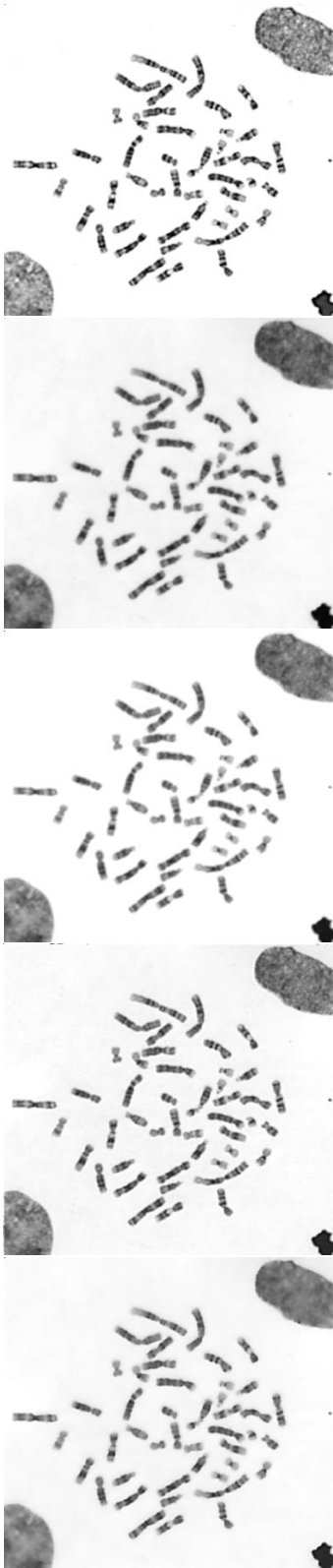
Fig. 10. A comparison of different methods for enhancing chromosome images in Fig. 1(a). From top to bottom: enhancement using the proposed method; MCE; CS; ACE and CGT, respectively.

21 [3]. Due to cell culture, staining and imaging condition, the metaphase spread images captured by microscopy need to be enhanced prior to feature extraction and classification.
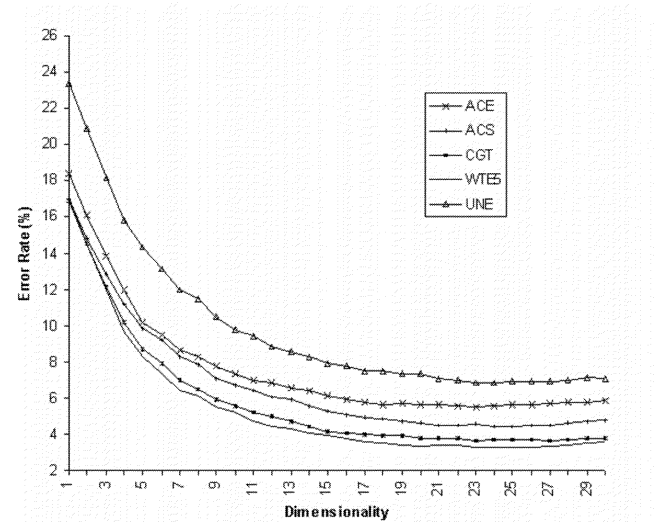

Fig. 11. Error rate curves of the classification as a function of number of features used. The methods tested are: ACE; CGT, ACS, unenhanced image (UNE), and the proposed wavelet-based approach (WTES).

For this purpose, we use the Bayesian classifier for chromosome classification. For objective comparisons the chromosome features are extracted using the same measurement procedure. The features used in this study include normalized length, density, density centrometric index (arm ratio), and weighted density distribution measurements from each chromosome [29]. The images were collected from a data archive at Dyna-Gene Cytogenetics Laboratories, Houston, TX and are fairly representative of routine sample quality. The dataset has 342 G-banded cells containing 15 136 chromosomes [29]. The classification results following different enhancement algorithms are plotted in Fig. 11. It is evident that the images enhanced by the proposed method result in the lowest classification error rate, which decreases as the dimensionality of feature space increases. These results indicate that enhanced images with the proposed method appear to provide more useful information and yield higher accuracy of classification. Hence, it will likely benefit cytogenetic diagnosis because chromosome abnormalities tend to be detected more effectively when the karyotyping accuracy improves.

VI. CONCLUSION

In this paper, we apply a class of differential wavelets [2] to chromosome image enhancement. It can also be used for general image contrast improvement. The proposed wavelets have several advantages for image enhancement. First, they are derived from splines and can be implemented efficiently. Second, the transforms are shift invariant and, thus, facilitate the measurement of correlation of image features in the transform domain. Third, the differential wavelet representations provide high-frequency edge information along horizontal, vertical, and diagonal directions. We exploit such directional edge information in the design of an image-enhancement algorithm. The disadvantage of this approach is the increased memory requirement due to the over-complete representations.

The proposed image-enhancement algorithm actually makes use of the information in the domain of the differential wavelet representation for extrapolation. Due to this type of wavelet representation, high-frequency features such as edges are characterized. We can tailor the algorithm to make the images not only sharper but also less noisy, so that they become visually appealing to the cytogeneticist.

The proposed enhancement algorithm has achieved objective improvement with medical significance in terms of qualitative contrast improvement and classification of chromosomes. Therefore, this technique provides a useful tool to assist clinicians in diagnosis and research.

A Java script demo program has been written to provide users with an interactive environment to test the method using their own images. The address of the java program is http://www.adires.com/09/index.shtml

References

[1] Y.-P. Wang and S. L. Lee, "Scale-space derived from b-splines," *IEEE Trans. Pattern Anal. and Machine Intell.*, vol. 20, no. 10, pp. 1050–1065, Oct. 1998.

[2] Y.-P. Wang, "Image representations using multiscale differential operators," *IEEE Trans. Image Processing*, vol. 8, pp. 1757–1771, Dec. 1999.

[3] Q. Wu, "Automated identification of human chromosomes as an exercise in building intelligent image recognition systems," Ph.D. dissertation, Katholieke Universiteit Leuven, Leuven, Belgium, 1991.

[4] Q. Wu and K. R. Castleman, "Multiscale image enhancement of chromosome banding patterns," *Proc. SPIE*, vol. 2825, pp. 796–804, 1996.

[5] A. K. Jain, *Digital Image Processing*. Englewood Cliffs, NJ: Prentice-Hall, 1989.

[6] K. S. Song, J. K. Kim, J. M. Park, and H. W. Park, "Adaptive mammographic image enhancement using first derivative and local statistics," *IEEE Trans. Med. Imag.*, vol. 16, pp. 495–502, Oct. 1997.

[7] C. H. Anderson, H. Greenspan, and S. Akber, "Image enhancement by nonlinear extrapolation in frequency space," *IEEE Trans. Image Processing*, vol. 9, pp. 1035–1048, June 2000.

[8] A. Polesel, G. Ramponi, and V. J. Mathews, "Image enhancement via adaptive unsharp masking," *IEEE Trans. Image Processing*, vol. 9, pp. 505–510, Mar. 2000.

[9] J. Lu and D. M. Healy, Jr., "Contrast enhancement via multiscale gradient transformation," in *Proc. IEEE Int. Conf. Image Processing*, Austin, TX, Nov. 1994, pp. 482–486.

[10] A. Laine, X. Zong, and E. Geiser, "Speckle reduction and contrast enhancement of echocardiograms via multiscale nonlinear processing," *IEEE Trans. Med. Imag.*, vol. 17, pp. 532–540, Aug. 1998.

[11] A. Laine, I. Koren, and F. Taylor, "Enhancement via fusion of mammographic features," in *Proc. Int. Conf. Image Processing*, vol. 2, Chicago, IL, Oct. 1998, pp. 722–726.

[12] H. C. Lien, J. C. Fu, and S. T. C. Wong, "Wavelet-based histogram equalization enhancment of gastric sonogram images," *Comput. Med. Imag. Graph.*, vol. 24, pp. 59–68, 2000.

[13] Y. Xu, B. Weaver, D. M. Healy, and J. Lu, "Wavelet domain filters: A spatial selective noise filtration technique," *IEEE Trans. Image Processing*, vol. 3, pp. 747–757, Nov. 1994.

[14] R. R. Coifman and D. L. Donoho, "Translation-invariant de-noising," in *Wavelets and Statistics*, A. Antoniadis and G. Oppenheim, Eds. Berlin, Germany: Springer-Verlag, 1995.

[15] C. B. Ahn, Y. C. Song, and D. J. Park, "Adaptive template filtering for signal-to-noise ratio enhancement in magnetic resonance imaging," *IEEE Trans. Med. Imag.*, vol. 18, pp. 549–556, June 1999.

[16] M. Unser, "Splines: A perfect fit for signal and image processing," *IEEE Signal Processing Mag.*, vol. 16, pp. 22–38, 1999.

[17] Y.-P. Wang, S. L. Lee, and K. Torachi, "Multiscale curvature-based shape representation using b-spline wavelets," *IEEE Trans. Image Processing*, vol. 8, pp. 1586–1592, Nov. 1999.

[18] B. M. Sadler and A. Swami, "Analysis of multiscale products for step detection and estimation," *IEEE Trans. Inform. Theory*, vol. 45, pp. 1043–1051, Apr. 1999.

[19] S. Mallat and S. Zhong, "Characterization of signals from multiscale edges," *IEEE Trans. Pattern Anal. Machine Intell.*, vol. 14, pp. 710–732, July 1992.

[20] A. Rosenfeld, "A nonlinear edge detection technique," *Proc. IEEE.*, pp. 814–816, 1970.

[21] A. Rosenfeld and M. Thurston, "Edge and curve detection for visual scene analysis," *IEEE Trans. Comput.*, vol. C-20, pp. 562–569, 1971.

[22] S. Mallat, "A theory for multiresolution signal decomposition: Wavelet representation," *IEEE Trans. Pattern Anal. Machine Intell.*, vol. 11, pp. 674–693, July 1989.

[23] D. Donoho and I. Johnstone, "Ideal spatial adaptation via wavelet shrinkage," *Biometrika*, vol. 81, pp. 425–455, 1994.

[24] S. K. Mitra and H. Li, "A new class of nonlinear filters for image enhancement," in *Proc. IEEE ICASSP*, Toronto, ON, Canada, 1991, pp. 2525–2528.

[25] A. Beghdadi and A. Le Negrate, "Contrast enhancement technique based on local detection of edges," *Comput. Vis. Graph. Image Proc.*, vol. 46, pp. 162–174, 1989.

[26] R. Gordon and R. M. Rangayyan, "Feature enhancement of film mammograms using fixed and adaptive neighborhoods," *Appl. Opt.*, vol. 23, no. 4, pp. 560–564, 1984.

[27] D.-C. Chang and W.-R. Wu, "Image contrast enhancement based on a histogram transformation of local standard deviation," *IEEE Trans. Med. Imag.*, vol. 17, pp. 518–531, Aug. 1998.

[28] G. Boccignone and M. Ferraro, "Multiscale contrast enhancement," *Electron. Lett.*, vol. 37, no. 2, pp. 751–752, 2001.

[29] Q. Wu, Y. Wang, Z. Liu, T. Chen, and K. R. Castleman, "The effect of image enhancement on biomedical pattern recognition," presented at the *2nd Joint IEEE EMBS-BMES Conf.*, Houston, TX, Oct. 23–26, 2002.